ENSO Index Variations and Links with Solar and Volcanic Activity

Valentina V. Zharkova[1,2], Irina Vasilieva[2,3]

[1]Department of MPEE, Faculty of Engineering and Environment, University of Northumbria, Newcastle upon Tyne, NE, UK; [2]ZVS Research Enterprise Ltd., London, UK; [3]Department of Solar Physics, Main Astronomical Observatory, Kyiv, Ukraine

Correspondence to: Valentina V. Zharkova, valentina.zharkova@northumbria.ac.uk ; Irina Vasilieva,
 valja46@gmail.com

ABSTRACT

In this paper, we investigated the Oceanic Niño Index (ONI), for simplicity called in this paper an El Nino Southern Oscillation (ENSO) index in 1950-2023 by applying the wavelet spectral transform and the IBM SPSS correlations analysis. ONI follows the three months' current measurements of the average temperature of the sea surface in the East-Central tropical part of the Pacific Ocean nearby the international line of the date change over the average sea surface temperature over the past 30 years. The ENSO index is found to have a strong (>87%) correlation with the Global Land-Ocean Temperature (GLOT). The scatter plots of the ENSO-GLOT correlation with the linear and cubic fits have shown that the ENSO index is better fit by the cubic polynomial increasing proportionally to a cubic power of the GLOT variations. The wavelet analysis allowed us to detect the two key periods in the ENSO (ONI) index: 4 - 5 years and 12 years. The smaller period of 4.5 years can be linked to the motion of tectonic plates while the larger period of 12 years is shown to have a noticeable correlation of 25% with frequencies of the underwater (submarine) volcanic eruptions in the areas with ENSO occurrences. Not withholding any local terrestrial factors considered to contribute to the ENSO occurrences, we investigated the possibility of the volcanic eruptions causing ENSO to be also induced by the tidal forces of Jupiter and Sun showing the correlation of the underwater volcanic eruption frequency with the Jupiter-Earth distances to be 12% and with the Sun-Earth distances, induced by the solar inertial motion, in January, when the Earth is turned to the Sun with the southern hemisphere where the ENSO occurs, to become 15%. Hence, the underwater volcanic eruptions induced by tidal forces of Jupiter and Sun can be the essential additional factors imposing this 12 year period of the ENSO (ONI) index variations.

1. INTRODUCTION

The El Nino Southern Oscillation (ENSO) phenomena are considered to be the most important events defining the modes of variability in the troposphere and influencing most parts of the world via teleconnection by providing significant impacts on precipitation in different parts of the globe [1]. The different types of ENSO occur to be likely defined by specific patterns of the sea surface temperature around tropical Pacific [2]. There is the EP-type, which is dominated in the East Pacific, and another type called CP, or Central Pacific, also called Modoki type [2-6]. The effects of each type of ENSO are rather different and require better understanding of the underlying forces producing these types of ENSO [1].

There are three evolution patterns identified for the Central-Pacific (CP) type of El Niño during 1958-2007: 1) a symmetric-decaying pattern whose sea surface temperature anomalies grow and decay symmetrically with respect to a peak phase; 2) a prolonged-decaying pattern that decays slowly and is followed by a warm event in the eastern Pacific (EP); and 3) an abrupt-decaying pattern that terminates rapidly after the peak and is followed by a cold event in the EP [2].

The depth of the equatorial thermocline is found to determine the type of evolution pattern to occur. If the CP El Niño occurs in a recharged thermocline state (*i.e.*, deeper-than-normal depth), an EP warming may appear in the decaying phase of the CP event to slow down the decay, giving rise to the prolonged-decaying pattern. If the thermocline is in a discharged state (*i.e.*, shallower-than-normal depth), an EP cooling may occur to abruptly terminate the CP El Niño. If the thermocline is in a neutral state (*i.e.*, normal depth), the CP event may have an asymmetric pattern of growth and decay. Although a few exceptions exist, these results indicate that the equatorial thermocline state at the peak phase of a CP El Niño event can be a potential predictor of the way the event may decay [2].

The origins of the delayed increases in global surface temperature accompanying El Nino and the implications for the role of adiabatic processes in El Nino-Southern Oscillation (ENSO) are explored by [3]. A major part of the ocean heat loss to the atmosphere is through evaporation and thus is released into the atmosphere as latent heating in precipitation, which drives teleconnections. Reduced precipitation and increased solar radiation in Australia, Southeast Asia, parts of Africa, and northern South America contribute to surface warming that peaks several months after the El Nino event. Teleconnections contribute to the extensive warming over Alaska and western Canada through a deeper Aleutian low and stronger southerly flow into these regions 0 - 12 months later.

CP ENSO phase transition (barrier, onset, etc.) happens in the spring and it is phase-locked with season; while for EP ENSO, the phase shift and barrier vary on a decade timescale [7]. There were two mechanisms for extratropical connections for CP ENSO proposed: Equatorial Ocean Advection Theory [8] and Extratropical Forcing Theory [2, 7, 9]. Based on the first theory, anomalous SST along the equatorial Pacific is grown by the zonal ocean advection, while the second theory suggests that it is initially excited by forcing from extra-tropics and then developed by the advection from the tropical ocean.

It was shown that atmospheric forcing plays the dominant role while for EP ENSO and it is mainly regulated by thermocline shifting [5]. Thermocline uplifting for El Niño (EN), while deepening down for La Niña (LN) is related to oceanic Kelvin and Rossby wave movement. That is the reason, the signal of phase reversal is detected only in EP ENSO, but CP ENSO occurs more as epochs or events rather than a cycle.

The 1976/1977 climate shift and the effects of two major volcanic eruptions in the past 2 decades were shown to be reflected in different evolution of ENSO events. At the surface, for 1979-1998 the warming in the central equatorial Pacific develops from the west and progresses eastward, while for 1950-1978 the anomalous warming begins along the coast of South America and spreads westward. The eastern Pacific South of the equator warms 4 - 8 months later for 1979-1998 but cools from 1950 to 1978 [3].

Yasuda [10] reported a statistically significant link between the ENSO timing and the 18.6-year period of the lunar tidal cycle in the mature-phase (December-February) ENSO time series during 1867-2015 and extending back to 1706 with proxy data. It was found that El-Niño tended to occur in the 1st, 10th, and 13th years after the maximum diurnal tide in the 18.6-yr cycle, and La-Niña tended to occur in the 3rd,

12th, and 16th years. These tendencies were also confirmed by corresponding sea-surface temperature (SST) and sea-level pressure (SLP) distributions; particularly Pacific SST and SLP spatial patterns in the third La-Niña and the tenth El-Niño year well resemble those of Pacific Decadal Oscillation (PDO).

The ENSO has definite effects on various regions around the world through teleconnection [11-13] influencing seasonal precipitation in different places including the Indian Summer Monsoon (ISM) [11, 14]. The ISM provides up to 80% of the annual mean precipitation, thus, making a significant impact on the Indian economy which is mainly dominated by agriculture and associated industries.

It is still not clear what phenomena or objects govern the appearance of ENSO. Since the Sun is the principal source of energy for the solar system one can expect its essential effect on the Earth climate. It has been shown that there is 0.1% - 1% variation in solar radiation in visible and UV ranges deposited to Earth between minimum to maximum years of the 11-year cycle [15-17]. This suggests that the variations in the solar UV spectrum between solar maxima and minima (6% to 8%) lead to more warming and ozone production during solar maxima in the upper region of the stratosphere [18].

Following thermal wind balance relationship, it is responsible for stronger (weaker) upper stratospheric jet for maximum (minimum) years. There are also changes in various dynamical features linked to such variability [13]. The timing is shown to be crucial to producing apparent discrepancies between different analyses of solar activity effects [19] identifying the solar cycle signals in 155 years of global sea level pressure (SLP) and sea surface temperature (SST) data using a multiple linear regression approach.

Recently, the solar activity was shown to be described not only by averaged sunspot numbers but also by eigenvectors of the solar background magnetic field (SBMF) derived with the principle component analysis (PCA) from the synoptic magnetic maps captured by the full-disk magnetograph of the Wilcox Solar Observatory, US [20]. This summary curve of these two PCs derived for cycles 21 - 23 and predicted for cycles 24 - 26 and for a few millennia [20] shows the temporal variations of the dominant eigenvectors of the solar background magnetic field. The modulus of the summary curve of the two principal components of SBMF fits rather closely with the averaged sunspot numbers currently used as the solar activity index [20-23].

The prediction of the summary curve to cycles 25 and 26 presented in Figure 2 in [20]) shows a noticeable decrease of the predicted average sunspot numbers in cycle 25 to ≈80% of that in cycle 24 and in cycle 26 to ≈40% that is linked to a reduction of the amplitudes and an increase of phases of the principal components of SBMF. The prediction of the summary curve by thousand years backward and forward presented in Figure 3 [20] revealed the occurrence of grand solar cycle of 350 - 400 years, reproducing the well-known Maunder, Wolf, Oort, Homeric and many other Grand Solar Minima.

During the most recent GSM, MM, there was a reduction for solar radiation [24] and the terrestrial temperature dropped by about 1C [25], which, in turn, was proxied by the absence of sunspots and active regions on the solar surface during the MM [26]. Currently, from cycle 21 the solar activity systematically decreased which coincided with a decrease of the solar background magnetic field in the approach of the GSM [20, 22].

The advantage of the new proxy of solar activity, the summary curve of two PCs, is provided by the fact that it not only provides the amplitudes and shapes of solar activity cycles but also captures the leading magnetic polarities in these cycles. Furthermore, by adding the other eigenvectors of SBMF linked to quadruple and sextuple magnetic field components, besides the two PCs associated with magnetic dipoles, it can replicate closer not only the sunspot index [20, 23] but also the soft X-ray flux index associated with solar flares [22].

On the other hand, in the past few hundred years, the Sun has been shown to provide some additional radiation to the Earth by moving closer toward the Earth's orbit because of the solar inertial motion (SIM) caused by the gravitation of the large planets [27-29]. These periodic variations of the Sun-Earth distance, and the solar irradiance, occur every 2100 - 2200 years, called Hallstatt's cycles, which were independently derived from the isotope abundances in the terrestrial biomass [30, 31]. In the current Hallstatt's millennial cycle, the Sun-Earth distances are decreasing from the MM until 2600 that leads to the increase of solar irradiance deposited to the atmosphere of the Earth (and other planets [28, 29].

This SIM effect is shown to contribute to the terrestrial atmosphere heating [28, 29], in addition to any heating considered in the terrestrial models. However, the most notable effect of the Sun in the next few decades will come from a reduction of solar activity, in spite of SIM or any other reason for global warming, that is caused by the modern grand solar minimum (GSM), which started in 2020 and will last until 2053 [20, 32].

The aim of the current study is to establish and understand better the key periods of ENSO index variations and investigate the characteristic periods of the occurrence of ENSO and find their possible links with the solar activity, solar magnetic field and solar position in its solar inertial motion.

2. ENSO OBSERVATIONS AND LINKS WITH SOLAR ACTIVITY

2.1. ENSO Dataset Description

The El Nino/La Nina Southern Oscillation (ENSO), e.g. the Niño 3.4 index, has been available since 1854 [33]. The Oceanic Niño Index (ONI) is taken from https://www.climate.gov/news-features/understanding-climate/climate-variability-oceanic-nino-index). ONI follows the three months current measurements of an average temperature of the sea surface in the East-Central tropical part of the Pacific ocean nearby the international line of the date change and demonstrates if these measurements show the ocean temperature to be colder or warmer than the averaged one over 30 years. In the current paper, for more transparent verbal visualisation in plots, we call this ONI as the ENSO index.

The temporal variations of this ENSO index from 1950 till present is shown in Figure 1, bottom plot, where the red colour shows the excesses above the averaged ENSO index and the blue colour shows the reductions below the averaged index. The top plot in Figure 1 shows the temporal variations of the Global Land-Ocean Temperature (GLOT) Index [34, 35]. It can be clearly noted from a comparison of the top and bottom plots that since 1950 onwards there is a visible link between the ENSO index and the increase of the GLOT. This point is investigated further in Section 3.1.

2.2. Links ENSO with Solar Activity Indices

The temporal variations of the ENSO index are compared in Figure 2 with variations of the solar activity indices measured by the averaged sunspot number (red curve) and the summary curve of the two largest eigenvectors derived from solar background magnetic field (SBMF) [20].

It can be seen that there is no clear correlation between the ENSO index neither with the averaged sunspot number index of solar activity shown by the red curve nor with the summary curve of eigenvectors of SBMF shown by the blue curve. To prove this statement we carried out a correlation analysis with the SPSS software of the ENSO index with 1) the averaged sunspot numbers index and 2) the summary curve of the eigenvectors and plotted their scatter plots with linear fits in Figure 3 in the top (for 1) and bottom (for 2) plots, respectively.

It can be seen that there is no noticeable correlation detected for the averaged sunspot number (Figure 3, top plot) with the correlation coefficient being 0.01, or 1%, e.g. close to zero. This is reflected in the linear fitting showing literally a straight line parallel to the axis X. Slightly better but still very low is the correlation of the ENSO index with the summary curve of SBMF (Figure 3, bottom plot), correlation coefficient is ≈0.1, or 10%. The ten-folded difference in the correlation coefficients of the ENSO with the sunspot numbers and SBMF can be easily understood from the comparison of these indices of solar activity [23], which highlighted the problems with the historic sunspot data to the favour of eigenvectors detected from the solar background magnetic field of the Sun.

Although let us mention that there is some response of the Pacific to the Sun's maxima of solar activity in cycles and contrasts to cold events in Southern Oscillation [36], in general, this allows us to think that solar activity may have some loose links to the ENSO index which are difficult to quantify though on a short-term 11-year timescale. One can conclude that the correlation of ENSO with solar activity indices
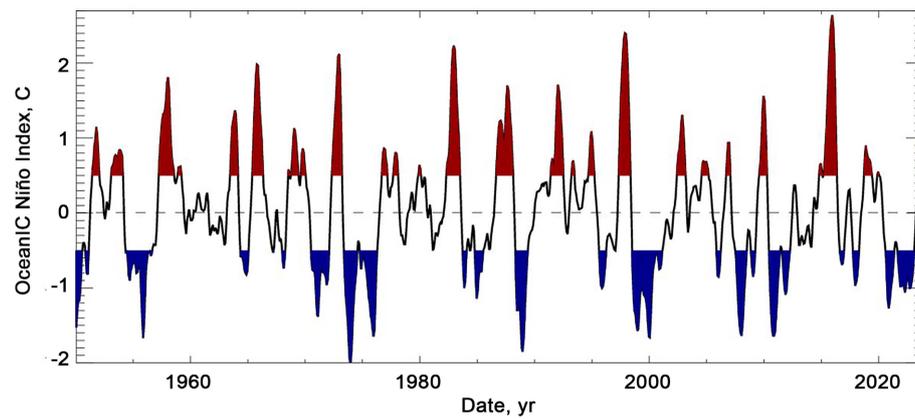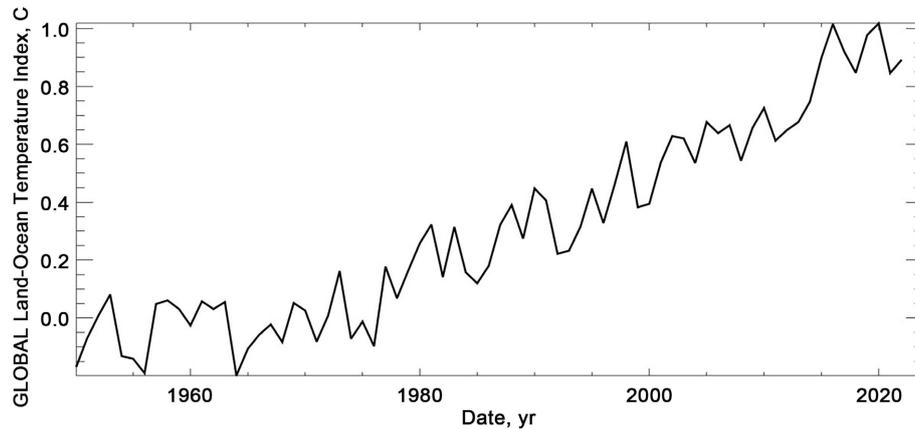
Figure 1. Top plot—Temporal variations of the combined land-surface air and sea-surface temperature, GLOT. Bottom plot—Temporal variations of the El Nina Southern Oscillation (ENSO) index. The red colour shows the excesses (hot periods) above the averaged ENSO index and blue colour shows the reductions (cold periods) below the averaged ENSO index (see the text for details).
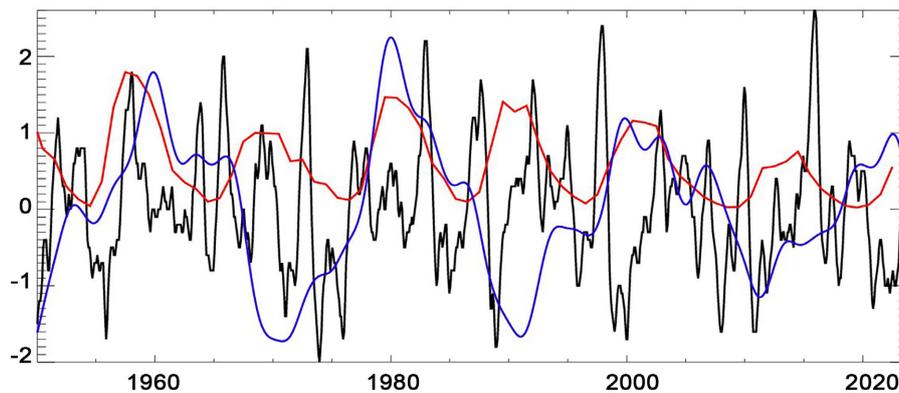
Figure 2. Comparison of temporal variations of the El Nina Southern Oscillation (ENSO) index with the averaged sunspot numbers (red curve) and the summary curve of eigenvectors of solar background magnetic field SBMF (blue curve).

Scatter plots of ENSO corrrelation with the averaged sunspot numbers

R^2 Linear = 8.180E-5

$y = -0.02 + 9.39E\text{-}5*X$

(a)

Scatter plots of ENSO corrrelation with the SBMF summary curve

R^2 Linear = 0.010

$y = -0.02 + 3.21E\text{-}4*X$
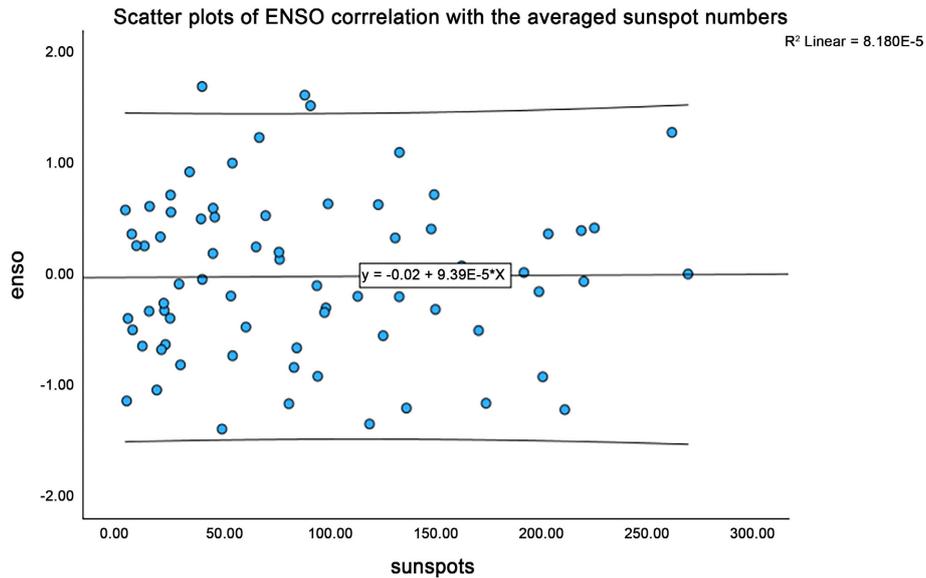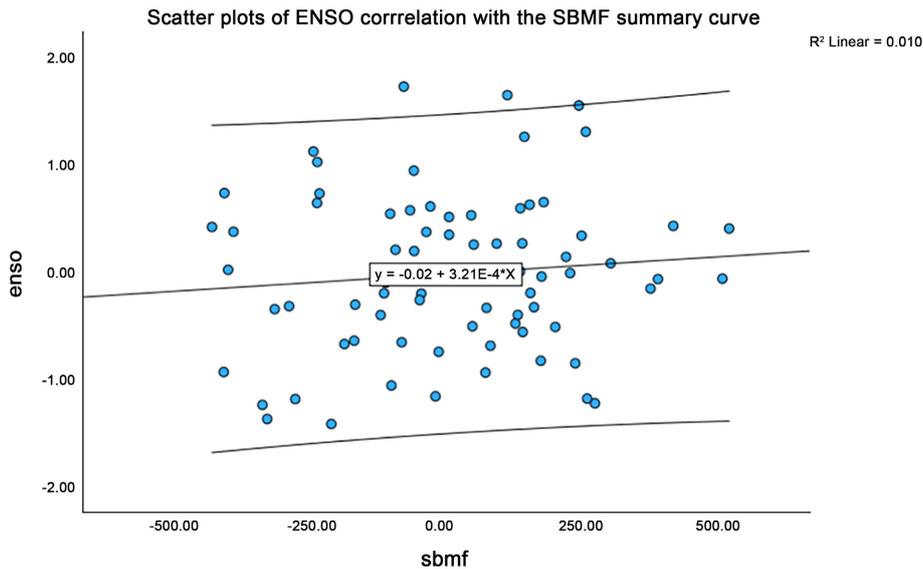
(b)

Figure 3. Scatter plots of the correlations carried with SPSS of the El Nina Southern Oscillation (ENSO) index with the averaged sunspot numbers, correlation coefficient of 0.009, (top plot) and with the summary curve of the eigenvectors of SBMF, correlation coefficient of 0.098, (bottom plot). The central lines in both plots present the linear fits of the correlation, the two thin outer lines indicate the 95% confidence interval of the fitting. The χ^2 of the linear fitting is presented in the top right corner of each plot.

is very weak and mostly associated with the solar magnetic field rather than with sunspots. Although, Roy and Haigh [19] have shown the solar cycle signals of 155 years in the global sea level pressure (SLP) and sea surface temperature (SST).

3. ANALYSIS OF THE ENSO DATA

3.1. Correlation Analysis of the ENSO and Temperature Indices

Let us now correlate the Global Land-Ocean terrestrial temperature (GLOT) with the temporal variations of the annual ENSO index from 1950 till present shown by the red curve in **Figure 1**, bottom plot. For this purpose, we run the correlation analysis (Pearson for normal data and Spearman for multivariate data) using the IBM SPSS Statistics package https://www.ibm.com/products/spss-statistics.

The SPSS correlation analysis of the ENSO index and GLOT temperature (top plot) presented in **Figure 4**, bottom plot reveals rather high correlation coefficients of 0.876 for Pearson correlation and 0.863 for Spearman one with a very high significance level P < 0.001. The scatter plots of the correlation analysis are presented in **Figure 5** with the top plot showing a fitting of the correlation curve by linear polynomial and the bottom plot—by cubic polynomial. (central black curves). The outer black curves show the 96% confidence interval for this regression fitting.

It can be noted that the very close correlation of the ENSO index with the Global Land-Ocean temperature (GLOT) variations, which is fit either by the linear ($\chi^2 = 0.768$) or by cubic ($\chi^2 = 0.778$) increase of the ENSO index in line with an increase of the GLOT temperature. Both linear and cubic fittings indicate a strong dependence on the ENSO index, or the sea temperature, which defines the intensity of the Southern Oscillation in the areas of its origin and its reflection via teleconnection to other parts of the globe. This fitting enhances the role of Henry's law in containment and depositions of deposition to the air of greenhouse gasses like CO_2 from the ocean waters [37, 38] with an increase in the ocean temperature and the correlating ENSO index.

3.2. Wavelet Analysis

3.2.1. Method Description

Wavelet transform of signals is the spectral analysis method providing a two-dimensional scan of the analysed signal (time and frequency, or period), in which the coordinates of the time and frequency are independent variables [39]. This representation allows one to explore the properties of the signal simultaneously in time and frequency domains. This makes the wavelet analysis an excellent tool for examining the series with time-varying frequency characteristics [39]. By considering the time series in the frequency-time space it is possible to derive dominant periods and their variations in time. The mother wavelet was selected as the Morlet wavelet (the real part of it is damped function of cosine), because with this choice one can obtain a high frequency resolution, which is important for our task.

The power of the wavelet spectra is shown in plots with wavelets by a colour bar plotted next to the wavelet spectrum. The Cone of Influence (COI) marked in the wavelet spectrum by the black dashed line, defines the parts of the spectrum with the essential border effects in the starting and finishing parts of the time series, because of a limited statistical data (boarder effects). Consequently, the results outside the COI are excluded from the further investigation, particularly, in the calculations of the global wavelet spectrum shown by the black curves on the right hand side from the wavelet spectra where we present by the solid black lines the global wavelet spectra integrated over time. The black dashed lines in the global wavelet plots present 95% confidence interval for the global wavelet spectrum.

3.2.2. Spectral Features of the ENSO Index Variations

In order to evaluate the spectral properties of the ENSO series and to derive the key periods, let us apply the Morlet wavelet analysis to both temperature sets with the results presented in **Figure 6** for the ENSO index shown in the top left plot, the ENSO wavelet spectrum shown in the bottom left plot and the ENSO global wavelet spectrum shown in the bottom right plot.

The most important feature derived from this series of the ENSO index is a presence of statistically significant periods of 3.57 - 5.05 and 12 years with some tendency to have a double 12-year period restricted by the ENSO data short length. The lower period of 4 - 5 years in the ENSO index variation is likely to be related to the tectonic plate movements [40] linked either to the variations of the local conditions
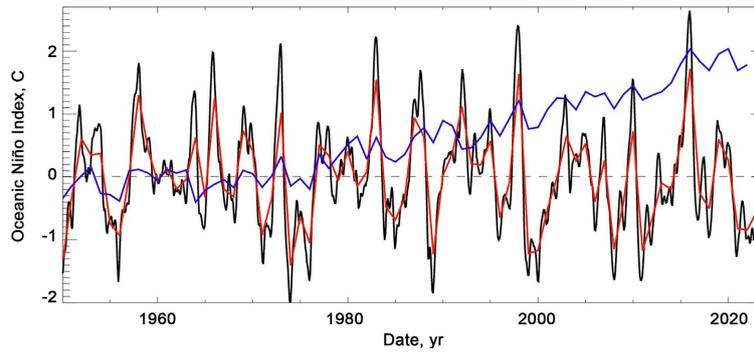
Figure 4. The temporal variations of the monthly El Nina Southern Oscillation (ENSO) index (black curve), of the annual ENSO index variations (red curve) and the global land-ocean terrestrial temperature (blue curve).
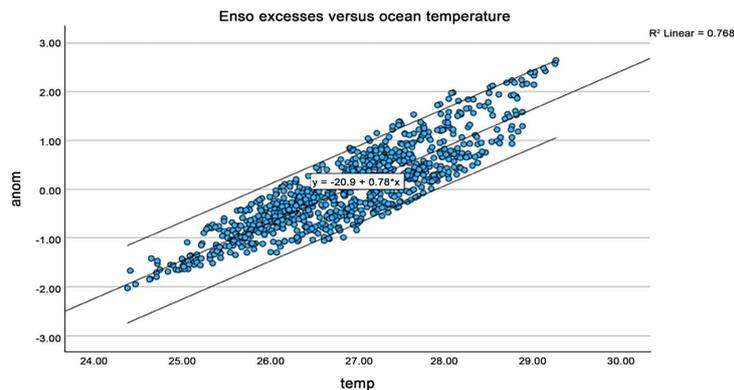
(a)
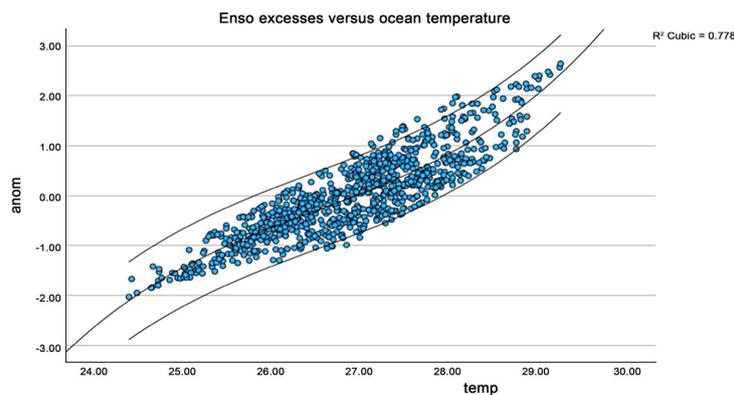
(b)

Figure 5. Scatter plots of correlation of the ENSO index variations and the global land-ocean temperature (GLOT) approximated by linear (central line, top plot) and cubic (central line, bottom plot) polynomials. The χ^2 of the linear fitting is presented in the top right corner of each plot. The outer thin lines define the 95% confidence intervals in each fit, the χ^2 coefficients of (0.768 for linear and 0.778 for cubic) regression fits are presented in the top right corners. The Pearson and Spearman correlation coefficients calculated for normal and multivariate data are equal to 0.887 and 0.863, respectively, with a significance level of P < 0.001.
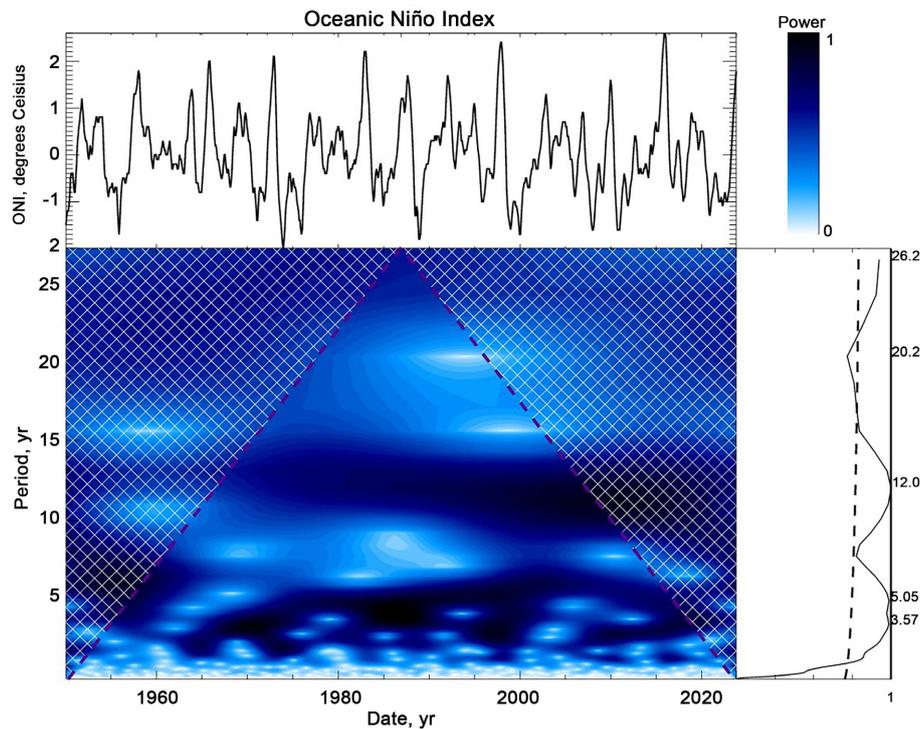
Figure 6. Wavelet analysis of the El Nina Southern temperature variations (ENSO) (top left plot). The wavelet spectrum of the ENSO temperature (bottom left plot) with the wavelet power marked by the colour bar (the top right plot). The bottom right plot shows the global wavelet spectrum of the ENSO index (black solid line) with the 95% confidence interval of the detected spectral features marked by the black dashed line).

in the ocean through Brewer-Dobson circulation and dominant positive Antarctic Oscillation (AAO) [13] or to increase of underwater volcanic activity [5, 40]. This extra-hearing caused by tectonic movement is expected to heat further the warm waters of the ocean leading to formation of strong ENSO.

The most puzzling is the larger period of 12 years in the ENSO index, which is detected with a high accuracy within 95% confidence interval. This period is not clearly linked to any solar activity indices shown in Section 2.2, which within in the same duration of the data have a period of about 10.7 years [23, 29]. Hence, this 12-year period of the ENSO index oscillation is outside the standard effects of solar activity as was also clearly shown in the previous Section 2.2.

3.3. Links of the ENSO Occurrences with Volcanic Eruptions

It has been noticed that the increases in ENSO index often coincide with the occurrences of volcanic activity in the ocean and around [5, 40]. The frequencies of volcanic eruptions over the Globe were found to be strongly linked to the variations of the summary curve of the two largest eigenvectors of solar background magnetic field (SBMF) [41]. Let us investigate now how this link can be associated with the variations of ENSO, which have a very weak correlation of 10% with this summary curve of SBMF as reported in Section 2.2.

Let us consider the locations of volcanic eruptions linked with ENSO. in **Figure 7**, top plot, we present by blue colour the areas of volcanic eruptions in the whole planet [41] and by yellow colour the locations of eruptions in the ENSO locations. In **Figure 7**, bottom plot, we present a comparison of temporal
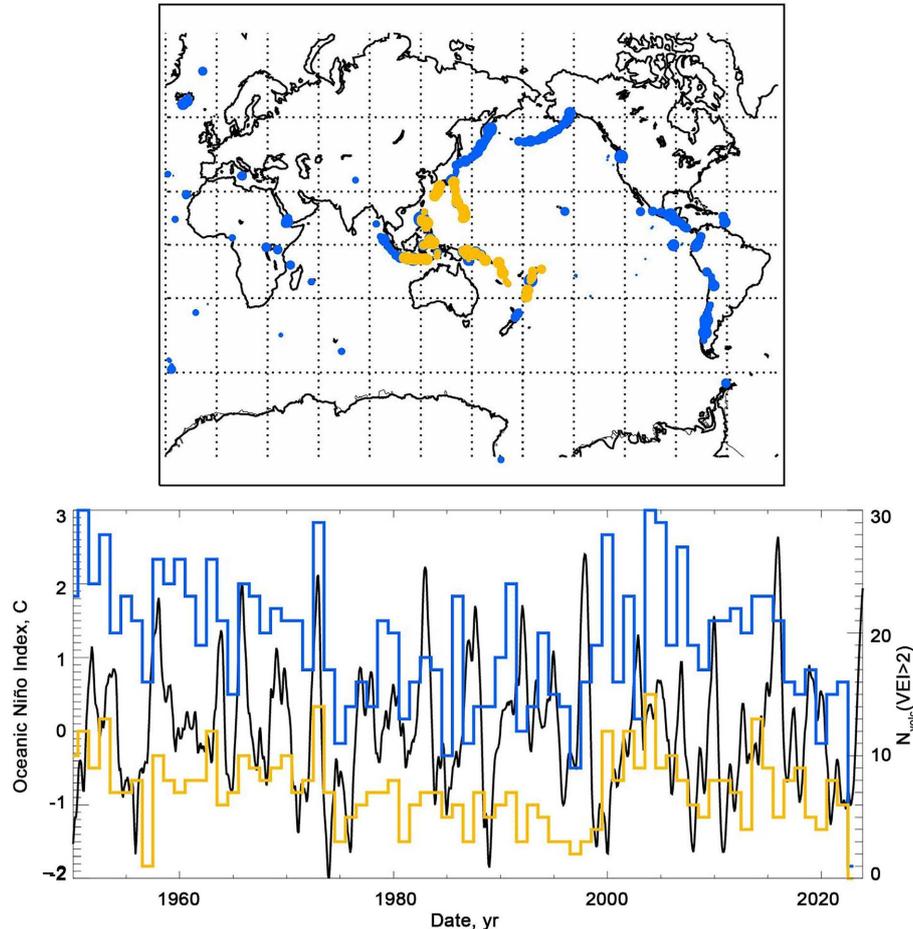
Figure 7. Links of the ENSO index to volcanic eruptions. Top plot: presents the geographical locations of volcanic eruptions with those occurred in the ENSO locations marked by the yellow colour. Bottom plot: shows temporal variations of ENSO index variations (black line) versus frequencies of volcanic eruptions with the index VEI > 2 per year in 1950-2023 for the whole volcanic data (blue line) and for the volcanic (surface and underwater, or submarine) eruptions in the locations of the ENSO occurrences (yellow plot). Taken from the area in the top plot marked by yellow colour.

variations of the ENSO index with the temporal variations of all the volcanic eruptions with the index VEI ≥ 2 (marked in blue colour) and with the volcanic eruptions taken from the locations of the ENSO occurrences (marked in yellow colour).

Logically speaking, only the volcanic eruptions in the ENSO areas can affect the occurrences of ENSO. Furthermore, in reality, the most contribution comes from the underwater (submarine) volcanic eruptions as suggested by a few authors [5, 40]. Hence we consider both the surface and underwater volcanic eruptions in the ENSO area.

In total, we used 137 underwater volcanic eruptions with 29 volcanos with the 0 < VEI < 4 located in the ENSO occurrence areas as shown In Figure 7 during the period of 1950 to 2023 years. Maximal volcanic index VEI = 4 was for the eruption of volcano Home Reef which lasted from 13.08.2021 till 12.09.2021 (31 days). Although, the majority of eruptions were from the volcanos with VEI = 0. The peak

in 1975 year was defined by the eruption of the volcano Fukutoku-Oka-no-Ba, which started in 1974 and lasted for the whole 1975 year. The dates and duration of eruptions of the submarine (underwater) volcanos with their names are shown in Figure 8, top plot.

For more accurate consideration of the underwater volcanic eruptions on the ocean temperature, one needs to consider the power of volcanic eruptions and their durations. We reckon that it is useful to use the duration and strength of volcanic eruptions as they indicate a real power of the ocean water heating by each eruption. For this reason, we introduced the new volcanic *Index*, which includes the power and duration of volcanos as follows:

$$\text{Index}\left(\text{year}\right) = \sum_{\text{volcano}} \left(2^{VEI_{\text{eruption}}} * \frac{N_{\text{day of eruption}}}{N_{\text{day of year}}} \right), \tag{1}$$

where $\sum_{\text{volcano}}$—a sum of all numbers of volcanic eruption in a given year, VEI_{eruption}—maximal index VEI of volcanic eruption in a given year, $N_{\text{day of eruption}}$—a number of days when eruption occurred, $N_{\text{day of year}}$—a number of days in a year (365 or 366). This volcanic index from Equation (1) (marked by the red line) is compared with the ENSO index (marked by the black line) in Figure 8, bottom plot.

In order to establish some quantified links between the presented indices, the correlation analysis was run with the SPSS software between the ENSO index (black curve) and total volcanic eruptions (blue curve) in Figure 7, bottom plot as well as the ENSO index (black curve) and frequency of submarine volcanic eruptions (yellow curve).

If we assume that the thermal energy deposited during a volcanic eruption is increased twice in the VEI increased by one and taking into account the duration of each eruption during a year. Then by summating the energy deposited by each volcano which had eruptions during the given year we calculate the energy deposited in this year by volcanic eruptions shown by the red curve versus ENSO index (black curve) in Figure 8, bottom plot. It can be seen these two curves of ENSO and underwater volcanic heating have rather close links.

The scatter plot of the correlation of the iENSO index and underwater volcanic index defined by Equation (1) is shown in Figure 9 indicating the linear increase of the ENSO index with the increase of the underwater index covering all the data within 95% confidence interval. We found a weak correlation of 12% between the ENSO and the total number of volcanic eruptions, and a twice higher correlation of 25% between the ENSO index and the underwater volcanic eruptions index defined by Equation (1). This confirms rather significant involvements of the underwater volcanic eruptions in formation of the ENSO phenomena, in addition to any other local influences mentioned in the introduction.

The reason for such boost of the ENSO index caused by volcanic eruptions some authors suggested to be the tidal force of the Moon [10]. However, the period of Moon revolution about the Earth cannot be linked to the 12-year period detected in the ENSO index with the wavelet spectral analysis. Although the search for any physical bodies which can have such clear periodicity has brought us to the period of Jupiter revolution about the barycentre of the solar system and about the Earth that will be discussed below in Section 3.4.

3.4. Possible Effects of Jupiter on the ENSO Index

3.4.1. Dependence of Volcanic Eruptions on Distances of Earth from Jupiter

In this section we do not consider various local terrestrial factors considered to contribute to the ENSO occurrences as discussed in the introduction. Instead, we attempt to investigate a role on the planet Earth of the tidal forces induced by the planet Jupiter in the positions where the largest number of volcanic eruptions occur. The frequency of volcanic eruptions as a function from the Earth-Jupiter distance is plotted in Figure 10 showing a total number of volcanic eruptions (blue line) and the eruptions that occurred in the ENSO occurrence area (yellow line). The mean eruptions for both types of volcanic eruptions are shown by the dashed lines of the relevant colours.

It can be seen clearly in Figure 10 that there are two specific distances to the planet Jupiter where the numbers of volcanic eruptions are the largest exceeding significantly, e.g. well above the mean numbers
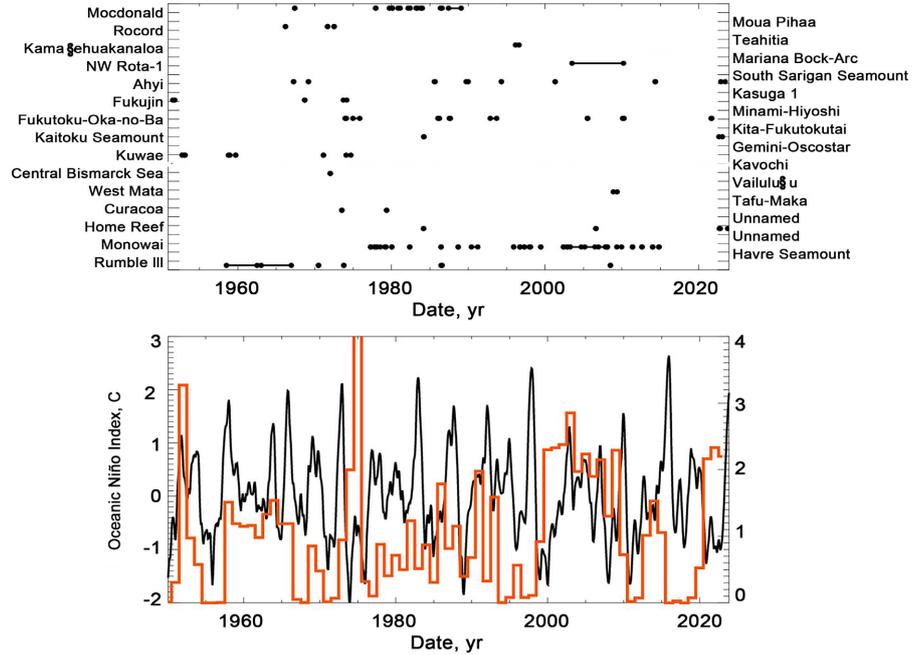
Figure 8. Top plot: The known submarine underwater volcanic eruptions with their durations. Bottom plot: The temporal variations of ENSO index (black curve) versus the submarine (underwater) volcanic eruptions (red curve) with the index VEI > 0 including the volcanic strength and duration, which is calculated as a fraction of the number of eruption days to the whole year duration by taking into account the power of eruption (see the text for more details).
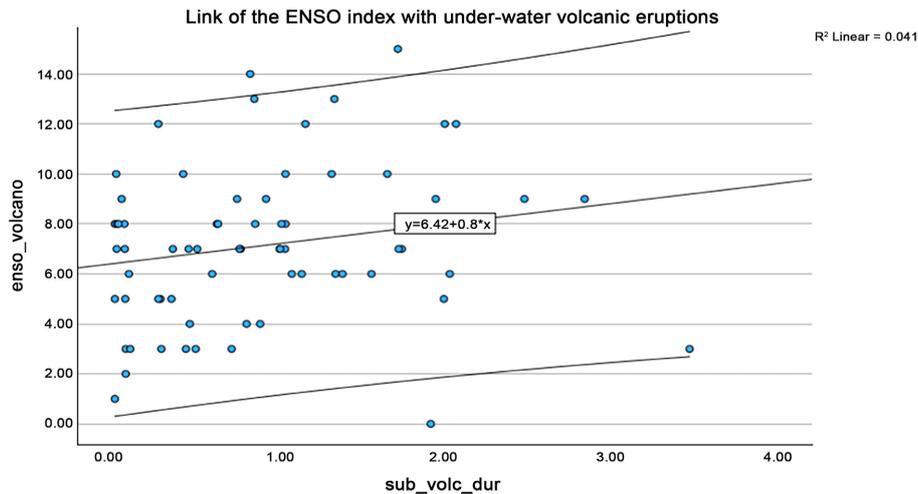
Figure 9. Scatter plot of the correlation (coefficient of 0,25) of the ENSO index with a frequency of the submarine volcanic eruptions having the index VEI< 2 including the eruption duration. The χ^2 of the linear fitting is presented in the top right corner of each plot. The central line presents a linear fit of the data, the outer lines show 95% confidence interval of the regression fit.
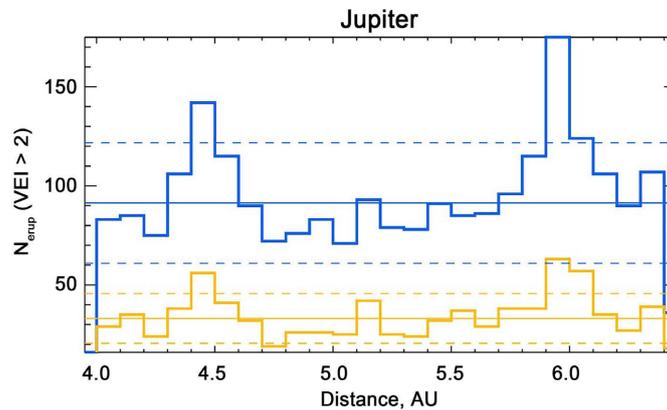
Figure 10. Frequencies of volcanic eruptions versus the distance (au) of Earth from Jupiter. The thick solid blue line shows the frequency of all volcanic eruptions, the thin solid blue line shows the mean number of all the volcanic eruptions, the dashed blue lines show the interval of standard deviation of the distances. The thick solid yellow line shows the frequency of volcanic eruptions occurring in the ENSO area, the thin yellow line shows the mean number of eruptions at a given time while the dashed yellow line marks the standard deviation interval for the distances.

and the standard deviation intervals shown by the thin lines of the relevant colours for either the volcanic eruptions (blue lines) or those eruptions in the ENSO area (yellow lines). These distances are 4.5 au when Jupiter is closest to the Earth and 6 au is when Jupiter is further from the Earth but the Sun becomes closest to the Earth in its inertial motion while appearing between the Earth and Jupiter.

It occurs that the Sun and Jupiter play an important gravitational role in initiating the volcanic eruptions on the Earth surface and underwater. These underwater volcanic eruptions can significantly heat the ocean waters and lead to large increases of ENSO during the periods of 5 - 6 and 12 years derived from the spectral analysis of ENSO in Section 3.2.

3.4.2. Links of ENSO Occurrences with Jupiter Distances

In order to clarify the role of gravitational forces caused by a close location of Jupiter to the Earth on the ENSO occurrences, let us compare the latter with the distances of Earth-Jupiter shown in **Figure 11**. It can be seen that indeed there is some visible element of correlation between these two curves which is confirmed statistically with Spearman correlation analysis with a correlation of 0.12 carried with the IBM SPSS software.

The scatter plot of this correlation is shown in **Figure 12**, which reveals a weak linear dependence of the ENSO index on the distance of Earth from Jupiter, possibly linked to the increased numbers of volcanic eruptions caused by its tidal forces.

3.4.3. Links of ENSO with the Distance to Sun

The effect of the solar system planet gravitation on the motion even of the star of the system, the Sun, leading to the solar inertial motion (SIM) about the barycentre of the solar system, has been reported by many authors [42-44] while only recently these effects have been linked to the changes in Sun-Earth distances on the orbit in different years, centuries or even millennia reporting the two-millennial variations of solar irradiance (Hallstaat's cycle) caused by SIM [27-29]. In this millennium the Sun is shown to move closer to the Earth's orbit during passing the orbit about the spring equinox in the Northern hemisphere.
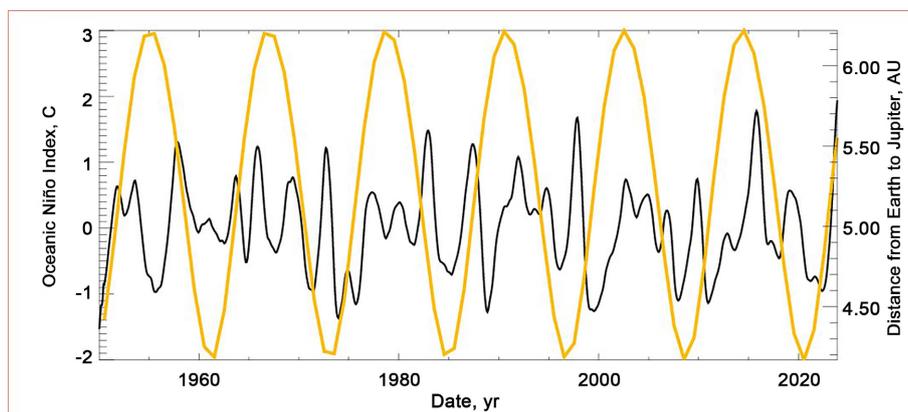
Figure 11. Temporal variations of the ENSO index (black curve) versus the distance (au) between the Earth and Jupiter taken from the official Horizon ephemeris (NASA) (yellow curve).
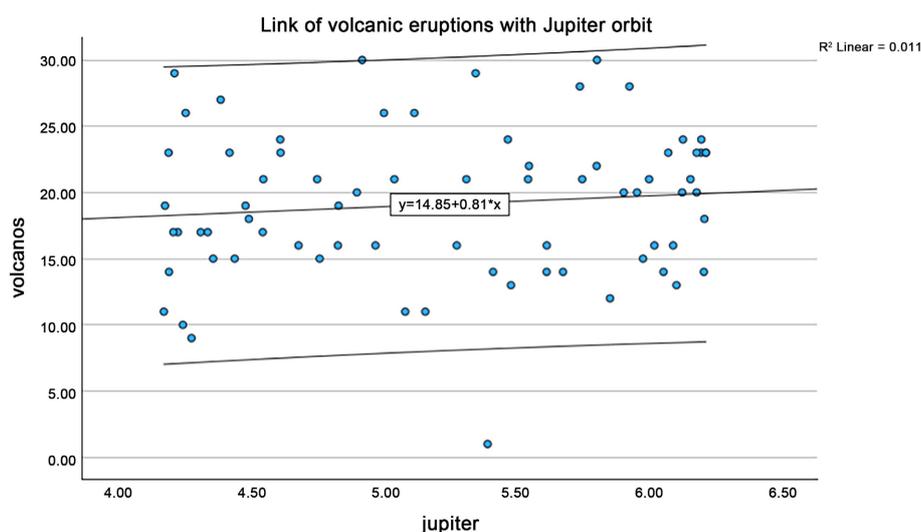
Figure 12. Scatter plot of a weak correlation (coefficient 0.12) of the ENSO index with the distance (au) between the Earth and Jupiter taken from the official Horizon ephemeris (NASA). The central line presents a linear fit of the data, the outer lines show 95% confidence interval of the fit.

Based on the topology of SIM and the asymmetry of distances between the Sun and Earth in the summer and winter months, let us compare the ENSO index with the distances between the Earth and Jupiter taken from the official Horizon ephemeris (NASA) measured on 15 January and 15 July of each year as presented in Figure 13.

It was noted that there was no noticeable correlation recorded between the ENSO index and the Sun-Earth distances in July. This is fully understandable since for this connection the closest part to the Sun on Earth is the Northern hemisphere and not the Southern one where the ENSO occurs. However, there is much significant connection has been established between the ENSO index and the Sun-Earth distance in January possibly linked to the underwater volcanic eruptions discussed in Section 3.3.

The scatter plot of the correlation (coefficient of 15%) of the ENSO index with a distance (au) between the Earth and Sun taken from the official Horizon ephemeris (NASA) in January of each year is
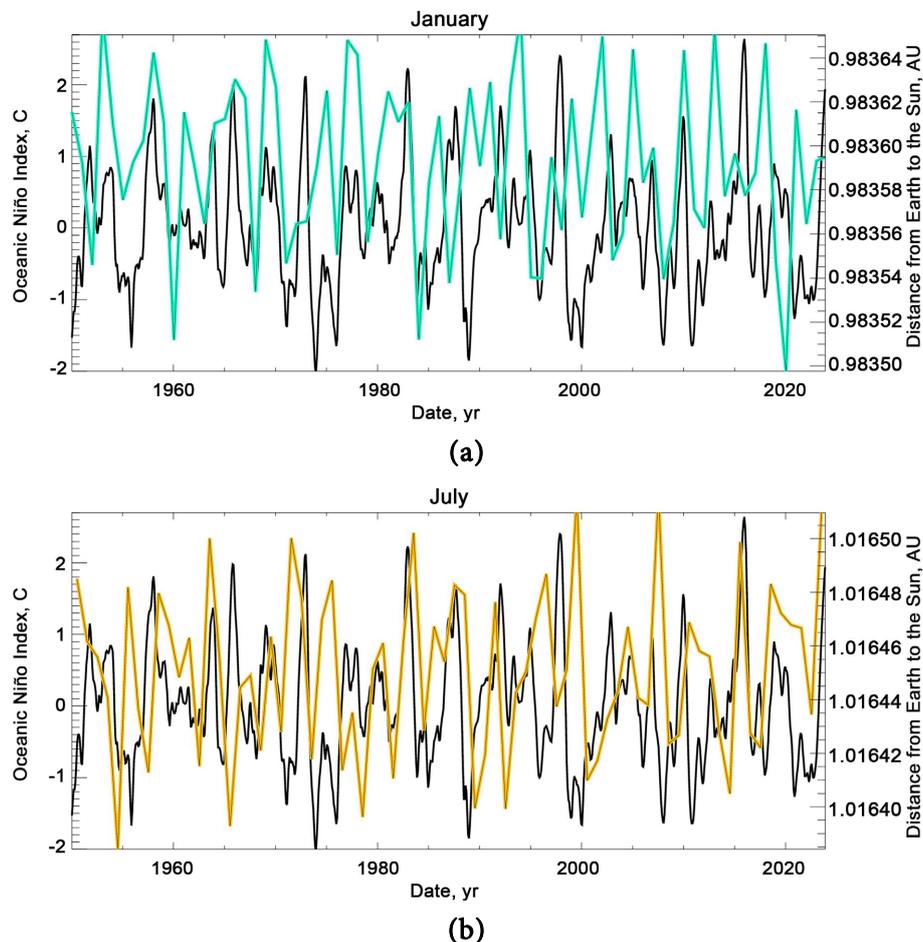
Figure 13. Comparison of the variations of the El Nina Southern Oscillation (ENSO) variations (black curve) and the distance of the Sun from the Earth taken from the official Horizon ephemeris (NASA) measured a) top plot: on 15 January of every year (cyan curve) and b) bottom plot: on the 15 July of each year (yellow curve).

shown in Figure 14. The central line presents a linear fit of the data, the outer lines show 95% confidence interval of the fit. It can be seen that during the times of January of each year when the Earth is turned to the Sun with the southern hemisphere where ENSO is formed, the correlation coefficient grows to 15% compared to 12% derived for the closest distance from Jupiter. This indicates that the Sun's gravitation can play an important role in initiating volcanic eruptions, similar to the gravitation of Jupiter, which is followed by the ENSO events increase.

4. DISCUSSION AND CONCLUSIONS

In this paper, we explored the links of the variations of the ENSO index with the terrestrial temperature, both solar activity indices defined by sunspots and SBMF and volcanic eruption frequencies in the areas of ENSO.

The increase of ENSO index above the average sea temperature magnitude, evaluated using the SPSS software is found to be very closely correlated (correlation coefficient of >0.87) to the global terrestrial temperature GLOT with ENSO index increasing as a cubic function of the temperature that indicates a significant link between level of ENSO and the GLOT.
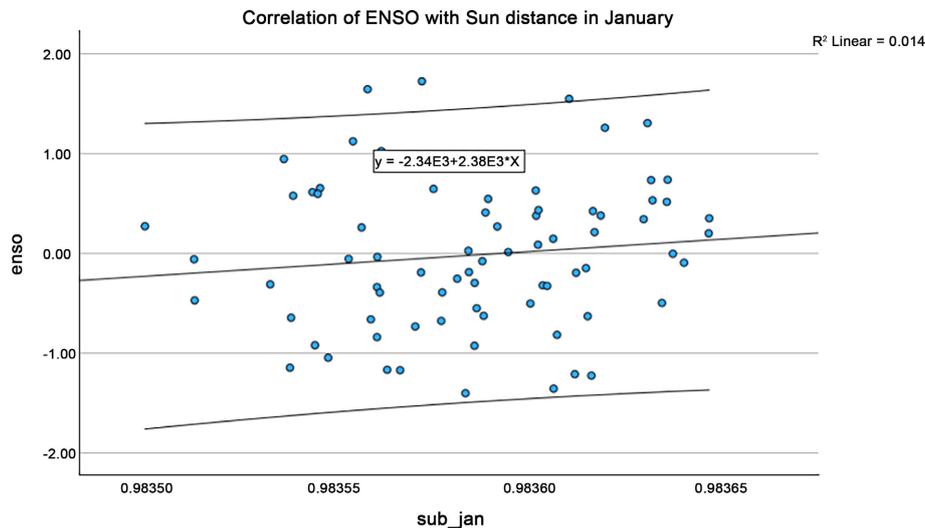
Figure 14. Scatter plot of the correlation (coefficient of 0.15) of the ENSO index with a distance (au) between the Earth and Sun taken from the official Horizon ephemeris (NASA) in January of each year shown in axis X. The central line presents a linear fit of the data, the outer lines show 95% confidence interval of the fit.

At the same time, we did not manage to establish clear links between the ENSO index variations and solar activity indices on 11-year timescale defined either by the averaged sunspot numbers or by the modulus summary curve of the two largest eigenvectors of SBMF. Although, there was a ten-folded difference in the correlation coefficients of the ENSO with the sunspot numbers (1%) and SBMF (10%) can be easily understood from the direct comparison of these indices of solar activity [23], which highlighted the problems with the historic sunspot data to the favour of eigenvectors detected from the solar background magnetic field of the Sun.

In order to find the essential periods of the ENSO index variations, we carried out our spectral analysis of the ENSO index with a wavelet transform and derived the two significant periods: 4 - 5 years and 12 years. The first period is likely to be related to the tectonic movement of the plates while the larger period of 12 years required more detailed investigation.

Based on the suggestions by a number of authors, we explored the dependence of the ENSO index on volcanic eruption frequencies in the whole globe and in the regions of ENSO assurances including the underwater, or submarine volcanos. The statistical study with IBM SPSS software revealed a noticeable correlation (25%) of the ENSO index with the frequency of occurrences of underwater volcanic eruptions that can cause significant heating of the deep water ocean, a delayed increase of the oceanic surface temperature while the hot waters travel to the surface and deposition of greenhouse gasses from the water following Henry's law.

We also explored possible links of the ENSO index variations with a 12-year period with the orbital motion of the Sun and Jupiter. We did not discuss any local terrestrial forces affecting ENSO, which were mentioned in the introduction and can play essential role in shaping the ENSO index in various parts of the Pacific. Instead, we try to derive a role of orbital motion which has a period of 12 years. We selected the planet Jupiter because of its period of rotation of 12 years which coincides with the largest period of the ENSO index oscillation reported in Section 3.2. The tidal forces from Moon have been already explored by some authors [10] but the effect of the tidal forces from Jupiter was not mentioned before.

At first, we explored the distances between Earth and Jupiter at which there are maximal numbers of volcanic eruptions occurring at distances of 4.5 au and 6 au. The shorter distance is well understood as the closest position of Jupiter to the Earth's southern hemisphere that can cause tidal force and initiate the

underwater and surface volcanic eruptions in the ENSO areas. This correlation of the distance between Jupiter and Earth is shown to be noticeable with a coefficient of 0.12 that is pretty high if taking into account the large distances between Earth and Jupiter.

The puzzling maximum at 6 au can be actually linked to the Sun's position towards the Earth caused by the gravitation of Jupiter, or solar inertial motion on a smaller time-scale. This correlation of the volcanic eruptions with the Sun-Earth distances can be tested by correlation with the distances measured in January when the Earth is turned to the Sun by the southern hemisphere where the ENSO occurs and in July when turned with the northern hemisphere. It turned out that the correlation with the July distances is negligible while the correlation with the distances of the Sun-Earth in January has coefficient of 0.15 which is higher than than that for the distance to Jupiter. The correlation coefficients of 12% and 15% for the distances from Jupiter and from the Sun, respectively, can explain the difference in the peaks of volcanic eruption frequencies reported for the Jupiter-Earth distances of 4.5 au and 6 au as shown in Figure 10.

Hence, in this paper, we have proven a strong (>0.87%) correlation of the ENSO (ONI) index with the Global Land-Ocean Temperature (GLOT) with the ENSO index to be likely increasing proportionally to a cubic power of the GLOT variations. The key periods of 4 - 5 years and 12 years were detected in the variations of the ENSO (ONI) index using the wavelet transform. We have shown a noticeable role of the underwater volcanic eruption in affecting the ENSO index variations and demonstrated the joint effect of orbital motion of Jupiter and Sun and their tidal forces can be the essential factors inducing this 12-year period of the ENSO (ONI) index variations.

ACKNOWLEDGMENTS

AUTHOR CONTRIBUTIONS STATEMENT

V.Z. formulated the problem, suggested the datasets to consider and analysis to carry out, did the calculations and analysis of the eigenvectors of the SBMF, did the statistical analysis with the IBM SPSS software, analysed the literature, designed the paper structure and produced the paper draft. I.V. gathered and processed the temperature, El Nino Southern Oscillation index, volcanic eruption, distance between the Sun/Jupiter and Earth, and carried the wavelet analysis. V.Z. and I.V. compared and analysed the results, wrote and reviewed the manuscript.

CONFLICTS OF INTEREST

The authors do not have any competing financial interests.

REFERENCES

1. Roy, I. and Kripalani, R.H. (2019) The Role of Natural Factors (Part 2): Indian Summer Monsoon in Climate Change Period—Observation and CMIP5 Models. *Theoretical and Applied Climatology*, **138**, 1525-1538. https://doi.org/10.1007/s00704-019-02864-2

2. Yu, J.-Y. and Kim, S.T. (2010) Identification of Central-Pacific and Eastern-Pacific Types of ENSO in CMIP3 Models. *Geophysics Research Letters*, **37**, L15705. https://doi.org/10.1029/2010GL044082

3. Trenberth, K.E., Caron J.M., Stepaniak, D.P. and Worley, S. (2002) Evolution of El Niño-Southern Oscillation and Global Atmospheric Surface Temperatures. *Journal of Geophysical Research* (*Atmospheres*), **107**, AAC

5-1-AAC 5-17. https://doi.org/10.1029/2000JD000298

4. Larkin, N.K. and Harrison, D.E. (2005) On the Definition of El Niño and Associated Seasonal Average U.S. Weather Anomalies. *Geophysics Research Letters*, **32**, L13705. https://doi.org/10.1029/2005GL022738

5. Ashok, K. and Yamagata, T. (2009) Climate Change: The El Niño with a Difference. *Nature*, **461**, 481-484. https://doi.org/10.1038/461481a

6. Hill, K.J., Taschetto, A.S. and England, M.H. (2009) South American Rainfall Impacts Associated with Inter-El Niño Variations. *Geophysics Research Letters*, **36**, L19702. https://doi.org/10.1029/2009GL040164

7. Kim, S.T. and Yu, J.-Y. (2012) The Two Types of ENSO in CMIP5 Models. *Geophysics Research Letters*, **39**, L11704. https://doi.org/10.1029/2012GL052006

8. Kug, J.-S., Ham, Y.-G., Jin, F.-F. and Kang, I.-S. (2010) Scale Interaction between Tropical Instability Waves and Low-Frequency Oceanic Flows. *Geophysics Research Letters*, **37**, L02710. https://doi.org/10.1029/2009GL041020

9. Yu, J.-Y. and Kim, S.T. (2010) Three Evolution Patterns of Central-Pacific El Niño. *Geophysics Research Letters*, **37**, L08706. https://doi.org/10.1029/2010GL042810

10. Yasuda, I. (2018) Impact of the Astronomical Lunar 18.6-Yr Tidal Cycle on El-Nino and Southern Oscillations. *Scientific Reports*, **8**, Article No. 15206. https://doi.org/10.1038/s41598-018-33526-4

11. Roy, I., Tedeschi, R.G. and Collins, M. (2017) ENSO Teleconnections to the Indian Summer Monsoon in Observations and Models. *EGU General Assembly Conference Abstracts*, Vienna, 23-28 April 2017, 1492.

12. Roy, I., Tedeschi, R.G. and Collins, M. (2017) ENSO Teleconnections to the Indian Summer Monsoon in Observations and Models. *International Journal of Climatology*, **37**, 1794-1813. https://doi.org/10.1002/joc.4811

13. Roy, I. (2018) Addressing on Abrupt Global Warming, Warming Trend Slowdown and Related Features in Recent Decades. *Frontiers in Earth Science*, **6**, Article No. 136. https://doi.org/10.3389/feart.2018.00136

14. Roy, I. and Tedeschi, R.G. (2016) Influence of ENSO on Regional Indian Summer Monsoon Precipitation—Local Atmospheric Influences or Remote Influence from Pacific. *Atmosphere*, **7**, Article No. 25. https://doi.org/10.3390/atmos7020025

15. Willson, R.C. and Hudson, H.S. (1991) The Sun's Luminosity over a Complete Solar Cycle. *Nature*, **351**, 42-44. https://doi.org/10.1038/351042a0

16. Lockwood, M., Stamper, R. and Wild, M.N. (1999) A Doubling of the Sun's Coronal Magnetic Field during the Past 100 Years. *Nature*, **399**, 437-439. https://doi.org/10.1038/20867

17. Fligge, M. and Solanki, S.K. (2000) The Solar Spectral Irradiance since 1700. *Geophysics Research Letters*, **27**, 2157-2160. https://doi.org/10.1029/2000GL000067

18. Crooks, S.A. and Gray, L.J. (2005) Characterization of the 11-Year Solar Signal Using a Multiple Regression Analysis of the ERA-40 Dataset. *Journal of Climate*, **18**, 996-1015. https://doi.org/10.1175/JCLI-3308.1

19. Roy, I. and Haigh, J.D. (2010) Solar Cycle Signals in Sea Level Pressure and Sea Surface Temperature. *Atmospheric Chemistry & Physics*, **10**, 3147-3153. https://doi.org/10.5194/acp-10-3147-2010

20. Zharkova, V.V., Shepherd, S.J., Popova, E. and Zharkov, S.I. (2015) Heartbeat of the Sun from Principal Component Analysis and Prediction of Solar Activity on a Millenium Timescale. *Scientific Reports*, **5**, Article No. 15689. https://doi.org/10.1038/srep15689

21. Shepherd, S.J., Zharkov, S.I. and Zharkova, V.V. (2014) Prediction of Solar Activity from Solar Background Magnetic Field Variations in Cycles 21-23. *The Astrophysical Journal*, **795**, Article No. 46. https://doi.org/10.1088/0004-637X/795/1/46

22. Zharkova, V.V. and Shepherd, S.J. (2022) Eigenvectors of Solar Magnetic Field in Cycles 21-24 and Their Links to Solar Activity Indices. *Monthly Notices of the Royal Astronomical Society*, **512**, 5085-5099.

https://doi.org/10.1093/mnras/stac781

23. Zharkova, V.V., Vasilieva, I., Popova, E. and Shepherd, S.J. (2023) Comparison of Solar Activity Proxies: Eigenvectors versus Averaged Sunspot Numbers. *Monthly Notices of the Royal Astronomical Society*, **521**, 6247-6265. https://doi.org/10.1093/mnras/stad1001

24. Lean, J., Beer, J. and Bradley, R. (1995) Reconstruction of Solar Irradiance since 1610: Implications for Climate Change. *Geophysical Research Letters*, **22**, 3195-3198. https://doi.org/10.1029/95GL03093

25. Easterbrook, D.J. (2016) Evidence-Based Climate Science. Elsevier, Amsterdam.

26. Eddy, J.A. (1976) The Maunder Minimum. *Science*, **192**, 1189-1202. https://doi.org/10.1126/science.192.4245.1189

27. Zharkova, V.V., Shepherd, S.J., Zharkov, S.I. and Popova, E. (2019) RETRACTED ARTICLE: Oscillations of the Baseline of Solar Magnetic Field and Solar Irradiance on a Millennial Timescale. *Scientific Reports*, **9**, Article No. 9197. https://doi.org/10.1038/s41598-019-45584-3

28. Zharkova, V. (2021) Millennial Oscillations of Solar Irradiance and Magnetic Field in 600-2600. In: Bevelacqua, J., Ed., *Solar System Planets and Exoplanets*, IntechOpen, London, 1-34. https://doi.org/10.5772/intechopen.96450

29. Zharkova, V.V., Vasilieva, I., Shepherd, S. and Popova, E. (2023) Periodicities of Solar Activity and Solar Radiation Derived from Observations and Their Links with the Terrestrial Environment. *Natural Science*, **15**, 111-147. https://doi.org/10.4236/ns.2023.153010

30. Steinhilber, F., Beer, J. and Fröhlich, C. (2009) Total Solar Irradiance during the Holocene. *Geophysical Research Letters*, **36**, L19704. https://doi.org/10.1029/2009GL040142

31. Steinhilber, F., Abreu, J.A., Beer, J., Brunner, I., Christl, M., Fischer, H., Heikkila, U., Kubik, P.W., Mann, M., McCracken, K.G., Miller, H., Miyahara, H., Oerter, H. and Wilhelms, F. (2012) 9,400 Years of Cosmic Radiation and Solar Activity from Ice Cores and Tree Rings. *Proceedings of the National Academy of Science*, **109**, 5967-5971. https://doi.org/10.1073/pnas.1118965109

32. Zharkova, V. (2020) Modern Grand Solar Minimum Will Lead to Terrestrial Cooling. *Temperature*, **7**, 217-222. https://doi.org/10.1080/23328940.2020.1796243

33. Kaplan, A., Cane, M.A., Kushnir, Y., Clement, A.C., Blumenthal, M.B. and Rajagopalan, B. (1998) Analyses of Global Sea Surface Temperature 1856-1991. *Journal of Geophysical Research*: *Oceans*, **103**, 18567-18589. https://doi.org/10.1029/97JC01736

34. GISTEMP Team (2024) GISS Surface Temperature Analysis (GISTEMP), Version 4. NASA Goddard Institute for Space Studies, New York.

35. Lenssen, N.J.L., Schmidt, G.A., Hansen, J.E., Menne, M.J., Persin, A., Ruedy, R. and Zyss, D. (2019) Improvements in the Gistemp Uncertainty Model. *Journal of Geophysical Research*: *Atmospheres*, **124**, 6307-6326. https://doi.org/10.1029/2018JD029522

36. Van Loon, H. and Meehl, G.A. (2008) The Response in the Pacific to the Sun's Decadal Peaks and Contrasts to Cold Events in the Southern Oscillation. *Journal of Atmospheric and Solar-Terrestrial Physics*, **70**, 1046-1055. https://doi.org/10.1016/j.jastp.2008.01.009

37. Henry, W. (1803) Experiments on the Quantity of Gases Absorbed by Water, at Different Temperatures, and under Different Pressures. *Philosophical Transactions of the Royal Society of London Series I*, **93**, 29-42+274. https://doi.org/10.1098/rstl.1803.0004

38. Sander, R., De Visscher, A.W.E.A., Schwartz, S.E. and Wallington, T.J. (2022) Henry's Law Constants (IUPAC Recommendations 2021). *Pure and Applied Chemistry*, **94**, 71-85. https://doi.org/10.1515/pac-2020-0302

39. Torrence, C. and Compo, G.P. (1998) A Practical Guide to Wavelet Analysis. *Bulletin of the American Meteo-*

rological Society, **79**, 61-78. https://doi.org/10.1175/1520-0477(1998)079<0061:APGTWA>2.0.CO;2

40. Van Westen, R.M., Kliphius, M. and Dukstraa, H.A. (2024) Physics-Based Early Warning Signal Shows That AMOC Is on Tipping Course. *Science Advances*, **10**, eadk1189. https://doi.org/10.1126/sciadv.adk1189

41. Vasilieva, I. and Zharkova, V. (2023) Terrestrial Volcanic Eruptions and Their Association with Solar Activity. *Global Journal of Science Frontier Research*, **23**, 22.

42. Charvatova, I. (1988) The Solar Motion and the Variability of Solar Activity. *Advances in Space Research*, **8**, 147-150. https://doi.org/10.1016/0273-1177(88)90184-6

43. Charvátová, I. (2000) Can Origin of the 2400-Year Cycle of Solar Activity Be Caused by Solar Inertial Motion? *Annales Geophysicae*, **18**, 399-405. https://doi.org/10.1007/s005850050897

44. Paluš, M., Kurths, J., Schwarz, U., Seehafer, N., Novotná, D. and Charvátová, I. (2007) The Solar Activity Cycle Is Weakly Synchronized with the Solar Inertial Motion. *Physics Letters A*, **365**, 421-428. https://doi.org/10.1016/j.physleta.2007.01.039